Analysis of aftershocks in a lithospheric model with seismogenic zone governed by damage rheology

Yehuda Ben-Zion[1] and Vladimir Lyakhovsky[2]

[1]*Department of Earth Sciences, University of Southern California Los Angeles, CA* 90089-0740, *USA. E-mail: benzion@usc.edu*
[2]*Geological Survey of Israel, Jerusalem* 95501, *Israel*

SUMMARY

We perform analytical and numerical studies of aftershock sequences following abrupt steps of strain in a rheologically layered model of the lithosphere. The model consists of a weak sedimentary layer, over a seismogenic zone governed by a viscoelastic damage rheology, underlain by a viscoelastic upper mantle. The damage rheology accounts for fundamental irreversible aspects of brittle rock deformation and is constrained by laboratory data of fracture and friction experiments. A 1-D version of the viscoelastic damage rheology leads to an exponential analytical solution for aftershock rates. The corresponding solution for a 3-D volume is expected to be sum of exponentials. The exponential solution depends primarily on a material parameter R given by the ratio of timescale for damage increase to timescale for accumulation of gradual inelastic deformation, and to a lesser extent on the initial damage and a threshold strain state for material degradation. The parameter R is also inversely proportional to the degree of seismic coupling across the fault. Simplifying the governing equations leads to a solution following the modified Omori power-law decay with an analytical exponent $p = 1$. In addition, the results associated with the general exponential expression can be fitted for various values of R with the modified Omori law. The same holds for the decay rates of aftershocks simulated numerically using the 3-D layered lithospheric model. The results indicate that low R values (e.g. $R \leq 1$) corresponding to cold brittle material produce long Omori-type aftershock sequences with high event productivity, while high R values (e.g. $R \geq 5$) corresponding to hot viscous material produce short diffuse response with low event productivity. The frequency-size statistics of aftershocks simulated in 3-D cases with low R values follow the Gutenberg–Richter power law relation, while events simulated for high R values are concentrated in a narrow magnitude range. Increasing thickness of the weak sedimentary cover produces results that are similar to those associated with higher R values. Increasing the assumed geothermal gradient reduces the depth extent of the simulated earthquakes. The magnitude of the largest simulated aftershocks is compatible with the Båth law for a range of values of a dynamic damage-weakening parameter. The results provide a physical basis for interpreting the main observed features of aftershock sequences in terms of basic structural and material properties.

Key words: aftershocks, cracked media, damage rheology, earthquake dynamics, fault mechanics, lithospheric model.

GJI Seismology

1 INTRODUCTION

Large earthquakes are typically followed by a period having an increasing number of earthquakes referred to as aftershocks. The main observed features of aftershock sequences (e.g. Kisslinger 1996; Utsu 2002) are as follows. (I) Aftershocks occur in a region around the main rupture zone that expands with time. (II) Their decay rate can be described (e.g. Utsu *et al.* 1995) by the modified Omori law

$$\Delta N / \Delta t = K(c + t)^{-p}, \tag{1}$$

where N is the cumulative number of events with magnitude larger than a prescribed cut-off, t is the time after the main shock, and K, c and p are empirical constants. Observed values of the exponent p are clustered around 1. However, aftershock decay rates can also be fitted (e.g. Gross & Kisslinger 1994; Narteau *et al.* 2002) with exponential and other functions. (III) The frequency-size statistics of aftershocks follow, like other regional earthquakes, the Gutenberg–Richter relation

$$\log N(M) = a - bM, \tag{2a}$$

197

where $N(M)$ is the number of events with magnitude larger than M and a, b are constants. Estimated b values of regional seismicity typically fall in the range 0.7–1.3. Eq. (2a) corresponds to a power-law probability function of the earthquakes potency values P_0

$$N(P_0) \propto P_0^{-\beta}, \tag{2b}$$

where P_0 is the integral of the final slip distribution over the failure area and $\beta = b/1.5$ (Ben-Zion 2003). Similar power-law probability functions characterize (Utsu 2002) the distribution of seismic moment (potency multiplied by the rigidity) and energy values of the events. (IV) The difference ΔM between the magnitude of the main shock and its largest aftershock is generally independent of the main shock magnitude (e.g. Båth 1965). The average ΔM values of aftershock sequences in a given region (e.g. southern California) are often close to 1. This is referred to as the Båth law. (V) The occurrence and properties of aftershocks exhibit a number of spatio-temporal variations that are unlikely to be associated with statistical fluctuations. These include the following. The depth extent of aftershocks is correlated with the geothermal gradient (Magistrale 2002) and the early parts of aftershock sequences may extend deeper than the regular ongoing seismicity (Rolandone *et al.* 2004). Cold continental regions with low heat flow have high aftershock productively and long event sequences associated with low effective power-law decay, while hot continental regions and oceanic lithosphere have low aftershock productively and short event sequences with fast decay (Kisslinger & Jones 1991; Davis & Frohlich 1991; Utsu *et al.* 1995; Kisslinger 1996; Boettcher & Jordan 2004; McGuire *et al.* 2005). Geothermal areas and volcanic regions with high fluid (magma, water) activity and high heat flow often have swarms of events without a clear separation between main shocks and aftershocks (Mogi 1967; Utsu 2002). In addition, observed b values of individual aftershock sequences can vary from 0.6 to 1.4 (e.g. Wiemer & Katsumata 1999) and observed values of ΔM associated with the Båth law can vary from 0.6 to 1.7 or more (e.g. Kisslinger & Jones 1991; Shcherbakov & Turcotte 2004).

In this work we attempt to establish a physical basis for understanding features (I)–(V), using a regional lithospheric model with a seismogenic crust governed by a continuum damage rheology that accounts for key observed features of irreversible rock deformation (Lyakhovsky *et al.* 1997a, 2005; Hamiel *et al.* 2004). A similar damage model was used by Shcherbakov *et al.* (2005) to derive a scaling relation for aftershocks that combines the modified Omori law and Gutenberg–Richter relation with the Båth law. Other physical models for aftershocks include rate-dependent creep rheology (Benioff 1951), migration of pore fluids (e.g. Nur & Booker 1972), stress corrosion (Das & Scholz 1981; Yamashita & Knopoff 1987), rate- and state-dependent friction (Dieterich 1994), and spatial variations of brittle and creep fault properties (Zöller *et al.* 2005). However, none of the existing models provides a unified explanation of properties (I)–(V), including the observed spatio-temporal variability of aftershock properties, in terms of basic geological and physical properties of the lithosphere. This is done in the present work with analytical and numerical parameter–space studies associated with our damage rheology framework and realistic model of the lithosphere.

In Section 2 of the paper we provide a review of the employed damage rheology model and lab-based constraints on the governing rheological parameters. In Section 3 we consider a simplified 1-D version of the model and derive an analytical solution for damage evolution during a relaxation process following an abrupt strain step. The solution provides guidelines for several expected properties of aftershock sequences. The analytical expression is associated with

an exponential function that depends on a single material parameter given by the ratio R between the timescale for damage increase in a fracture process and the timescale for accumulation of gradual inelastic deformation. Low values of R representing cold material with high viscosity produce a slow brittle relaxation process with long aftershock sequences, while high values of R representing hot low-viscosity material produce rapid relaxation with short aftershock sequences. The results generated by the analytical solution can be fitted well for various values of R with the modified Omori power-law relation.

In Section 4 of the paper we present results of 3-D numerical simulations in a regional lithospheric model consisting of a sedimentary layer, over a brittle seismogenic crust governed by the damage rheology, underlain by a viscoelastic upper mantle with power-law creep. The decay rates of aftershock sequences following abrupt loading steps, simulated with various values of R, are compatible with the analytical results. The frequency-size statistics of aftershocks simulated with relatively low R values follow the Gutenberg–Richter power-law distribution, while the statistics of events simulated with relatively high R values have a narrow range and cannot be described by a power-law relation. The largest aftershocks in simulations with dynamic weakening during brittle failures in a range of values are compatible with the Båth law. Increasing thickness of the weak sedimentary cover reduces the number of events and duration of the simulated aftershock sequences, similar to what is produced by increasing R value. Increasing temperature gradient reduces the depth extent of the aftershocks, but has a minor direct effect on the aftershocks duration. The maximum depth of aftershocks in a given model realization is initially high and decreases with time, reflecting a transient deepening of the brittle–ductile transition depth generated by the main shock. The implications of the results to aftershock sequences and other aspects of crustal deformation are discussed in Section 5.

2 A VISCOELASTIC DAMAGE RHEOLOGY MODEL

The damage rheology we use (Lyakhovsky *et al.* 1997a; Hamiel *et al.* 2004) accounts for the following three general aspects of brittle rock deformation under large irreversible strain.

(1) A mechanical aspect quantifying the dependency of the effective elastic moduli on the existing density of microcracks.

(2) A kinetic aspect quantifying the evolution of microcrack density (leading to degradation and recovery of the effective elastic moduli) with the ongoing deformation.

(3) Dynamical aspects modelling stable and unstable material failures associated with gradual accumulation of inelastic strain and brittle instability, respectively.

The theoretical developments are done within a non-linear continuum mechanics framework (e.g. Kachanov 1986; Rabotnov 1988), where the microcrack density is represented by an intensive damage state variable α. The results are applicable to volumes with a sufficiently large number of cracks that allow quantitative description through properties of the crack distribution rather than those of the individual cracks. Discrete models of damage associated with fibre bundles or other discrete elements can lead to similar results in the limit of a large number of elements (e.g. Krajcinovic 1996; Newman & Phoenix 2001; Turcotte *et al.* 2003).

Lyakhovsky *et al.* (1997b) modelled the effects of an existing crack population (damage) by generalizing the elastic strain energy

function of a deforming solid to the form

$$U = \frac{1}{\rho} \left(\frac{\lambda}{2} I_1^2 + \mu I_2 - \gamma I_1 \sqrt{I_2} \right), \tag{3}$$

where $I_1 = \varepsilon_{kk}$ and $I_2 = \varepsilon_{ij} \varepsilon_{ij}$ are the first and second invariants of the elastic strain tensor ε_{ij} (summation convention applied), λ and μ are the Lamé parameters of linear Hookean elasticity, and γ is a third modulus for a damaged solid. The result was obtained using the self-consistent formulation of Budiansky & O'Connell (1976) for non-interacting cracks that dilate and contract in response to tension and compression. Lyakhovsky *et al.* (1997b) showed that the dependency of the elastic potential on the third strain invariant $I_3 = \det(\varepsilon_{ij})$ is very weak and may be neglected. The obtained potential form is the simplest mathematical expression for the elastic strain energy that generalizes the classical potential to a non-analytical second-order function of two strain invariants I_1 and I_2.

The same result can be obtained by considering a general function for the strain energy having any second-order term of the type $I_1^{2x} \cdot I_2^{1-x}$ with $0 < x < 1$, and eliminating unphysical values of the exponents. The limit values $x = 0$ and $x = 1$ are associated with the Hookean first two terms of (3). The relation between the mean stress (σ_{kk}) and volumetric deformation (I_1) for the assumed general form is

$$\sigma_{kk} = \rho \frac{\partial U}{\partial I_1} \sim 2x I_1^{2x-1} I_2^{1-x} + \frac{2}{3}(1-x) I_1^{2x+1} I_2^{-x}. \tag{4}$$

The second term in eq. (4) is regular for every $0 < x < 1$, while the first term has a non-physical singularity for $0 < x < 1/2$. Only exponent values in the range $x \geq 1/2$ lead (in addition to $x = 0$) to a non-singular stress–strain relation. However, for $x > 1/2$ the volumetric strain is zero ($I_1 = 0$) for zero mean stress ($\sigma_{kk} = 0$) and any non-zero shear loading ($I_2 \neq 0$). This is not compatible with material dilation under shear loading, which is widely observed in rock deformation experiments (e.g. Jaeger & Cook 1976). Thus the only exponent (other than the classical 0 and 1 values) associated with realistic rock deformation is the $x = 1/2$ value represented by the third term in eq. (3).

The resulting stress–strain relation associated with the strain energy function (3) is

$$\sigma_{ij} = \rho \frac{\partial U}{\partial \varepsilon_{ij}} = \left(\lambda I_1 - \gamma \sqrt{I_2} \right) \delta_{ij} + \left(2\mu - \gamma \frac{I_1}{\sqrt{I_2}} \right) \varepsilon_{ij}. \tag{5}$$

Eq. (5) reduces to linear Hookean elasticity for an undamaged solid ($\gamma = 0$) and it describes non-linear elasticity for a damaged solid ($\gamma > 0$) with asymmetric response to loading under tension and compression conditions (Lyakhovsky *et al.* 1993, 1997b).

The kinetic aspect of the damage rheology model is accounted for by making the moduli λ, μ and γ functions of an evolving damage state variable $0 \leq \alpha \leq 1$ representing the local microcrack density. Using the balance equations of energy and entropy, and accounting for irreversible changes related to viscous deformation and material damage, the equation of damage evolution has the form (Lyakhovsky *et al.* 1997a)

$$\frac{d\alpha}{dt} = -C \frac{\partial U}{\partial \alpha}, \tag{6}$$

where the positive constant or function of state variables C produces non-negative local entropy production related to damage evolution. Eq. (6) can describe not only damage increase or material degradation, but also the process of material recovery associated with healing of microcracks. The latter is favoured by high confining pressure, low shear stress and high temperature.

Agnon & Lyakhovsky (1995) assumed for simplicity that the moduli μ and γ are linear functions of α and the modulus λ is constant. Later analysis of laboratory acoustic emission and stress–strain data (Hamiel *et al.* 2004) showed that the quality of data fitting may be improved by assuming power-law relations between α and the elastic moduli. However, assuming constant λ and using linear relations of μ and γ to α still provide good approximations for conditions of the seismogenic zone. Increasing the modulus γ from 0 for a damage-free Hookean solid to its maximum value at critical damage, amplifies the non-linearity of rock elasticity with damage accumulation.

Substituting the elastic strain energy (3) into (6), the equation for the kinetics of damage evolution is (Lyakhovsky *et al.* 1997a)

$$\frac{d\alpha}{dt} = \begin{cases} C_d I_2 (\xi - \xi_0), & \text{for } \xi \geq \xi_0 \\ C_1 \cdot \exp\left(\frac{\alpha}{C_2}\right) I_2 (\xi - \xi_0), & \text{for } \xi < \xi_0 \end{cases}, \tag{7}$$

where $\xi = I_1/\sqrt{I_2}$ is referred to as the strain invariants ratio. The parameter ξ_0 separates states of deformation involving material degradation and healing, associated with positive and negative damage evolution, respectively. Agnon & Lyakhovsky (1995) and Lyakhovsky *et al.* (1997a) related this parameter to the angle of internal friction by considering the critical shear stress for Mohr-Coulomb sliding. They obtained $\xi_0 = -0.8$ for typical ratios of elastic moduli for damage-free material $\lambda/\mu \approx 1$ (Poisson's ratio of about 0.25) and internal friction angle $\approx 40°$ (Eq. 37 and Fig. 3 of Lyakhovsky *et al.* 1997a). This value varies only slightly for rocks with Poisson ratios between 0.2 and 0.3 and is used in the numerical simulations of Section 4. The parameter C_d is a damage-rate constant for material degradation and it defines the timescale for the occurrence of a macroscopic brittle failure following the onset of positive damage evolution at $\xi = \xi_0$.

The initiation of brittle instability leading to macroscopic failure is associated in the model with loss of convexity of the strain energy function at a critical level α_c of the damage state variable (Lyakhovsky *et al.* 1997a). The critical level of damage for propagation of the instability is lower than the initiation level by a dynamic weakening factor discussed in the appendix. These conditions were used by Ben-Zion *et al.* (1999), Lyakhovsky *et al.* (2001a) and Ben-Zion & Lyakhovsky (2002) to calculate the initiation and propagation of seismic events in numerical simulations, and are also used in Section 4. Lyakhovsky *et al.* (1997a) suggested that C_d is a material constant and estimated its value to vary from 0.5 to $5\ \text{s}^{-1}$ for different rocks tested at relatively high confining pressures and room temperature. However, Lyakhovsky *et al.* (2005) showed that the damage model with a constant C_d significantly overestimates the strength of Westerly granite at low confining pressures, and suggested a pressure-dependent C_d that varies exponentially with a characteristic scale of 50 MPa. The obtained C_d is approximately constant for pressures above 50–100 MPa, indicating that for simulations of fracture processes at depth larger than about 3–5 km, where the bulk of seismic slip occurs, C_d may be taken as a constant. Lyakhovsky *et al.* (2005) also showed that the employed viscoelastic damage model, with the exponential healing in the kinetic eq. (7), reproduces the key observed features of rate- and state-dependent friction. A comparison of model calculations with observed values of the parameters a and b of the rate- and state-dependent friction allowed Lyakhovsky *et al.* (2005) to constrain the damage healing parameters C_1, C_2 of eq. (7).

Detailed analysis of laboratory data (Hamiel *et al.* 2004) showed that with the onset of acoustic emissions and positive damage evolution, a gradual irreversible (inelastic) strain accumulates before

the final macroscopic failure. In a Maxwell element the strains are additive, so the total strain is the sum of the elastic and inelastic components. Hamiel *et al.* (2004) suggested the rate of accumulation of gradual inelastic strain components e_{ij} is proportional to the rate of positive damage evolution $d\alpha/dt > 0$,

$$e_{ij} = C_v \frac{d\alpha}{dt} \tau_{ij}, \tag{8}$$

where $C_v \cdot d\alpha/dt$ is an effective damage-related ductile compliance, or the inverse of an effective damage-related viscosity, and τ_{ij} is the deviatoric stress tensor. The value of the effective viscosity increases with decreasing damage rate and becomes infinitely large (i.e. associated with zero viscous deformation) when the positive damage evolution approaches zero at the transition to healing. The physical unit of the coefficient C_v is inverse stress and does not introduce a new timescale to the viscoelastic damage rheology model. The timescale of all processes related to the positive damage evolution is controlled by the damage rate parameter C_d. Hamiel *et al.* (2004) presented 3-D numerical simulations based on the generalized version of the viscoelastic damage model with eq. (8). The results fitted well both the observed stress–strain curves and acoustic emission data of laboratory experiments with Westerly granite and Berea sandstone. The generalized version of the viscoelastic damage model with eqs (5), (7) and (8) is used in the sections below for analysis of aftershocks.

3 ANALYTICAL RESULTS FOR AFTERSHOCK DECAY RATES

The 3-D model formulation is simplified significantly for a 1-D version corresponding to uniform deformation, not accounting for the tensorial nature of deformation and spatial variations of properties or processes. In this section we consider such a case and derive analytical results that provide general expectations for aftershock decay rates.

While the general stress–strain relations (5) based on the elastic potential (3) are non-linear, the corresponding 1-D stress–strain relation has the linear form

$$\sigma = 2\mu_0(1 - \alpha)\varepsilon, \tag{9}$$

where $\mu_0(1 - \alpha)$ is the effective elastic modulus of a 1-D damaged material with μ_0 being the initial rigidity of the undamaged solid. The 1-D version of the kinetic eq. (7) for damage evolution is

$$\dot{\alpha} = C_d(\varepsilon^2 - \varepsilon_0^2), \tag{10}$$

where ε_0 is a threshold value separating states of strain associated with material degradation and healing. Shcherbakov *et al.* (2005) used a 1-D damage model similar to that associated with eqs (9) and (10), along with an assumed power-law dependency of C_d on the stress above a yielding stress level, to obtain a power-law scaling for aftershock rates. As discussed in Section 2, comparisons of model predictions with observed strength of Westerly granite indicate that C_d is approximately constant for conditions corresponding to depths larger than about 3–5 km (Lyakhovsky *et al.* 2005). Since the seismically active portion of the crust is generally below 3–5 km (e.g. Scholz 2002), we use here a constant C_d.

For positive damage evolution ($\varepsilon > \varepsilon_0$), the damage-related inelastic strain rate before the final macroscopic failure is given by

$$e = C_v \dot{\alpha} \sigma. \tag{11}$$

The set of eqs (9)–(11) governs the 1-D behaviour of the (spatially uniform) system. A similar set of equations with constant viscosity was analysed by Lyakhovsky *et al.* (1997a) to describe a stick-slip motion under a constant rate of applied deformation. Ben-Zion &

Lyakhovsky (2002) showed analytically that eqs (9) and (10) lead under constant stress, in a system without gradual inelastic strain accumulation and a constant C_d, to a power-law time-to-failure relation consistent with observed seismic activation before some large earthquakes. A similar derivation was obtained by Turcotte *et al.* (2003). The analytical result was confirmed by numerical simulations in a rheologically layered model with a seismogenic crust governed by the damage rheology (Ben-Zion & Lyakhovsky 2002). The assumed constant stress loading in those works provides an appropriate boundary condition for evolutionary deformation leading to a system-size event. Here we analyse the behaviour of a more general system, having both brittle and gradual inelastic components of deformation, subjected to a constant total strain boundary condition. Such a condition is appropriate for a relaxation process in a region following the occurrence of a large event.

The constant total strain condition implies that the rate of elastic strain relaxation is equal to the viscous strain rate, that is, $2 \cdot \dot{\varepsilon} = -e$. The factor 2 stems from the common definitions of the strain and strain-rate tensors, $\varepsilon_{ij} = (\partial u_i/\partial x_j + \partial u_j/\partial x_i)/2$, $e_{ij} = (\partial v_i/\partial x_j + \partial v_j/\partial x_i)$, where u_i and v_i are displacement and velocity components, respectively. Substituting this condition in (11) and then in (9) gives

$$\frac{d\varepsilon}{dt} = -C_v \mu_0 (1 - \alpha) \cdot \varepsilon \frac{d\alpha}{dt}. \tag{12}$$

Integrating (12) we get

$$\varepsilon = A \cdot \exp\left[\frac{1}{2} R (1 - \alpha)^2\right], \tag{13}$$

where $A = \varepsilon_s \cdot \exp[-\frac{1}{2} R(1 - \alpha_s)^2]$ is an integration constant with $\alpha = \alpha_s$ and $\varepsilon = \varepsilon_s$ for $t = 0$, and $R = \mu_0 \cdot C_v$ is a material parameter. As demonstrated below analytically and numerically, the parameter R plays a dominant role in the aftershock behaviour. Recalling that the damage-related viscosity is $\eta = 1/C_v \dot{\alpha}$, it is easy to show that R characterizes the ratio between a brittle damage timescale $\tau_d = 1/[C_d(\varepsilon^2 - \varepsilon_0^2)]$ and a Maxwell viscous timescale $\tau_M = \eta/\mu$. Substituting eq. (13) into eq. (10) leads to damage evolution following an exponential function

$$\frac{d\alpha}{dt} = C_d \cdot \left\{\varepsilon_s^2 \exp\left[R(1 - \alpha)^2 - R(1 - \alpha_s)^2\right] - \varepsilon_0^2\right\}. \tag{14}$$

To convert the evolution of the damage state variable α to evolution of aftershocks number N, we assume that α increases linearly with N,

$$\alpha = \alpha_s + \phi N. \tag{15}$$

We thus get

$$\phi \frac{dN}{dt} = C_d \cdot \left\{\varepsilon_s^2 \exp\left[R(1 - \alpha_s - \phi N)^2 - R(1 - \alpha_s)^2\right] - \varepsilon_0^2\right\}. \tag{16a}$$

The corresponding solution for a 3-D volume with many interacting elements is expected to be associated with a sum of exponentials similar to eq. (16a). We note that the solution of Dieterich (1994) for brittle deformation rate following a stress step, based on rate- and state-dependent friction, is also associated with an exponential function, and that Narteau *et al.* (2002) fitted observed aftershock sequences with sums of exponentials. For the limiting case with $\varepsilon_0 = 0$, eq. (16a) has a solution in the form

$$\mathrm{erf}[\sqrt{R}(1 - \alpha_s - \phi N)] = \mathrm{erf}[\sqrt{R}(1 - \alpha_s)]$$

$$- \exp[-R(1 - \alpha_s)^2]\sqrt{R} C_d \varepsilon_s^2 \frac{2}{\sqrt{\pi}} \cdot t. \tag{16b}$$
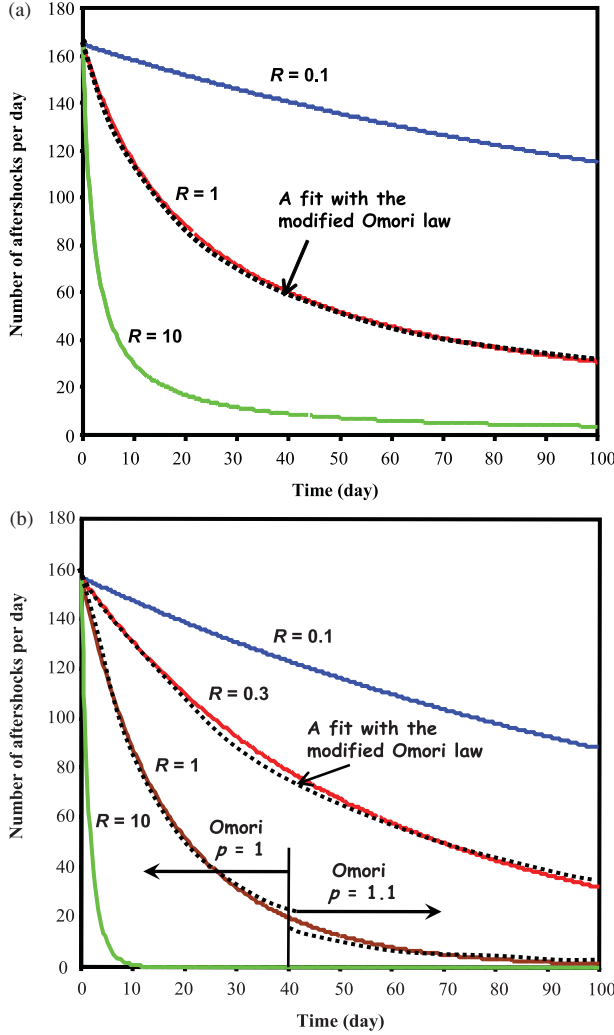
Figure 1. (a) Analytical results based on eq. (16a) for aftershock decay rates in a 1-D version of the damage model for different R values (lines with different colours). The dotted line is least-squares fit to the exponential analytical solution with the modified Omori power law (eq. 1). See text for additional parameters and explanations. (b) Additional cases of analytical exponential results and least-squares fits based on the modified Omori law. See text for parameters and explanations.

Fig. 1(a) shows the evolution of the number of aftershocks N per day based on eq. (16a) for several values of R (solid lines), using $C_d = 1\text{ s}^{-1}$, $\phi = 1.3 \times 10^{-4}$, $\varepsilon_s = 5.0 \times 10^{-4}$, and the simplifying limit values $\alpha_s = 0$ and $\varepsilon_0 = 0$. (Below we consider results associated with non-zero α_s and ε_0.) Seismological observations indicate that the average change of seismic velocity in a region during an aftershock sequence is on the order of 1 per cent or less, depending on the region being considered (e.g. Poupinet *et al.* 1984; Peng & Ben-Zion 2006). Thus, the scaling parameter ϕ governing the change of the average damage variable α during the occurrence of N aftershocks (eq. 15) should be very small. For example, with $\phi = 1.3 \times 10^{-4}$ the number of events in Fig. 1(a) during 100 days for R values of 10, 1 and 0.1 are about 1500, 6500 and 13 500, respectively. The corresponding relative changes to the shear wave velocity $\Delta\beta/\beta$ are about 10, 60 and more than 100 per cent, respectively. These changes are unrealistically high, except perhaps in some highly localized space–time regions.

As seen in Fig. 1(a), small R values, corresponding to highly brittle cases with little viscous relaxation, produce long aftershock sequences with slow decay and high aftershock productivity (e.g. $\sim10^4$ events in 100 days for the case $R = 0.1$). In contrast, high R values, corresponding to relatively viscous cases, produce short aftershock sequences with fast decay and low aftershock productivity ($\sim10^3$ events for $R = 10$). While the aftershock rates in Fig. 1(a) are generated using the exponential eq. (16a), the results can be fitted well by the modified Omori power-law relation $K(c + t)^{-p}$. This is illustrated for the case $R = 1$ with a line fit based on the modified Omori law (dotted black line) with $K = 1470$, $c = 14$ day and $p = 0.8$. Changing the power-law parameters we can produce reasonable fits to all three solid lines. We note that it is possible to obtain good fits to the results with several different sets of parameters [see, e.g. eq. (18c) for a relation between the c and K values for an analytical power-law version of our model], and that the examples shown only intend to illustrate general effects. More realistic cases of simulated aftershock sequences, and fitting values of the modified Omori law parameters, are given in Section 4 where we perform numerical simulations in a spatially heterogeneous 3-D volume having many interacting elements.

Fig. 1(b) gives the number of aftershocks per day for various cases of R (solid lines), using eq. (16a) with $C_d = 1\text{ s}^{-1}$, $\phi = 6.6 \times 10^{-6}$, $\varepsilon_s = 6 \times 10^{-4}$, $\alpha_s = 0.2$ and $\varepsilon_0 = 5 \times 10^{-4}$. Here the aftershock sequences during 100 days are associated with $N \approx 11\,800$ and $\Delta\beta/\beta \approx 60$ per cent for $R = 0.1$, $N \approx 7600$ and $\Delta\beta/\beta \approx 35$ per cent for $R = 0.3$, $N \approx 2900$ and $\Delta\beta/\beta \approx 12$ per cent for $R = 1$, and $N \approx 300$ and $\Delta\beta/\beta \approx 1$ per cent for $R = 10$. With the employed parameters, the results of Fig. 1(b) can be fitted well for the case $R = 0.3$ over the examined 100 days (dotted black line) using the modified Omori law with $K = 1800$, $c = 15$ day and $p = 0.8$ Obtaining good fits with the modified Omori law for cases with larger R values requires that we change the power-law parameters with time. For example, the case $R = 1$ is fitted (dotted black lines) with $K = 1120$, $c = 5.3$ day and $p = 1$ for the first 40 days, and $K = 800$, $c = 3$ day and $p = 1.1$ for the following 60 days. We note that analyses of observed aftershock sequences also indicate, at least in some cases, decay rates (or p values) that increase with time (e.g. Davis & Frohlich 1991; Narteau *et al.* 2002; Peng *et al.* 2006).

The obtained good fits to the curves of Figs 1(a) and (b) with lines based on the modified Omori law suggest that the leading term of eq. (16a) is associated with a power law. This can be derived explicitly by making the following two simplifications. Assuming that ϕN is sufficiently small so that the $(\phi N)^2$ term in (16a) can be neglected, gives

$$\phi\frac{dN}{dt} = C_d \cdot \left\{ \varepsilon_s^2 \exp\left[-2\phi NR(1 - \alpha_s)\right] - \varepsilon_0^2 \right\}. \qquad (17)$$

As discussed above, the assumption of very small ϕN is generally appropriate for a 1-D analysis of average changes associated with aftershock sequences. If we assume further that the initial strain ε_s induced by the main shock is large enough so that $\varepsilon_0^2 \ll \varepsilon_s^2 \exp\left[-2\phi NR(1 - \alpha_s)\right]$, we get

$$N = \frac{1}{2\phi R(1 - \alpha_s)} \ln\left[2R(1 - \alpha_s)C_d \varepsilon_s^2 t + 1\right]. \qquad (18a)$$

Eq. (18a) corresponds to the modified Omori law. This can be seen more clearly by rewriting the result as

$$\frac{dN}{dt} = \frac{\dot{N}_0}{2\phi R(1 - \alpha_s)\dot{N}_0 t + 1}$$
$$= \frac{\dot{N}_0}{2\phi R(1 - \alpha_s)\dot{N}_0} \cdot \frac{1}{t + 1/2\phi R(1 - \alpha_s)\dot{N}_0}, \qquad (18b)$$

where $\dot{N}_0 = C_d \varepsilon_s^2 / \phi$ is the initial aftershocks rate. Eq. (18b) provides a mapping between parameters of the modified Omori law and parameters of our damage rheology model (in a 1-D analysis of uniform deformation),

$$k = \frac{1}{2\phi R(1 - \alpha_s)},$$

$$c = \frac{1}{2\phi R(1 - \alpha_s)\dot{N}_0} = \frac{k}{\dot{N}_0},$$

$$p = 1. \tag{18c}$$

We recall that the logarithmic solution (18a) and power-law decay rate (18b) were obtained using the two assumptions (a) $\phi N \ll 1$ and (b) $\varepsilon_0^2 \ll \varepsilon_s^2 \exp[-2\phi NR(1 - \alpha_s)]$. These assumptions can not generally be satisfied simultaneously for a long period of time. The solution (18a) is compatible with condition (a) only for time intervals $t \ll 1/C_d \varepsilon_s^2$, and the right side of condition (b) decreases with increasing N (and hence increasing t). These conditions are compatible with the statement that the power-law version of our more general exponential function is the first term in a Taylor-Maclaurin expansion, and they explain why the modified Omori law can fit well only short intervals for the fast decaying cases in Fig. 1(b). If we drop condition (b), so that the results account for a finite ε_0 value, and proceed from eq. (17), the solution is

$$\ln\left\{\frac{\varepsilon_s^2 \exp[-2\phi NR(1 - \alpha_s)] - \varepsilon_0^2}{\varepsilon_s^2 - \varepsilon_0^2}\right\}$$

$$-2\phi NR(1 - \alpha_s) = C_d \varepsilon_0^2 2R(1 - \alpha_s) \cdot t. \tag{19}$$

In this case, the total number of events N_T from eq. (17) is $N_T = \ln(\varepsilon_s/\varepsilon_0)/(\phi R)$, and the value ϕN can remain small throughout the entire aftershock sequence for a ratio $\varepsilon_s/\varepsilon_0$ close to 1.

4 NUMERICAL RESULTS ON AFTERSHOCK PROPERTIES

To establish the conditions for which the analytical results are valid, and study additional properties of aftershock sequences, we perform 3-D numerical simulations in a rheologically layered model with a seismogenic layer governed by the viscoelastic damage rheology. The numerical simulations employ the Fast Lagrangian Analysis of Continua algorithm (Cundall & Board 1988; Cundall 1989; Poliakov *et al.* 1993). The 3-D numerical algorithm for the damage rheology model of Lyakhovsky *et al.* (2001b) was modified here to account for the accumulation of inelastic damage-related strain components and ductile flow discussed in the next section. The simulations are done with tetrahedral elements of variable sizes that increase gradually from about 500 m in the seismogenic zone to about 5 km in the ductile region. The mesh was generated with the TetGen code (by Hang Si from Research Group of Numerical Mathematics and Scientific Computing, Weierstrass Institute for Applied Analysis and Stochastic <http://tetgen.berlios.de>).

4.1 Model set-up

The 3-D numerical model consists of a rheologically layered structure with the three main units of a continental lithosphere (Fig. 2). The upper layer represents a top cover of weak sediments with a thickness of 1–7 km in different model realizations. Cases with a relatively thick top cover correspond to regions with deep sedimentary basins, such as in the Los Angeles, Ventura and Dead Sea areas. The second and third layers represent the crystalline crust and upper mantle, respectively. The interface between these layers is at a depth of 35 km, which is a typical Moho depth for continental crust. In the simulations below, the mass density, initial shear modulus
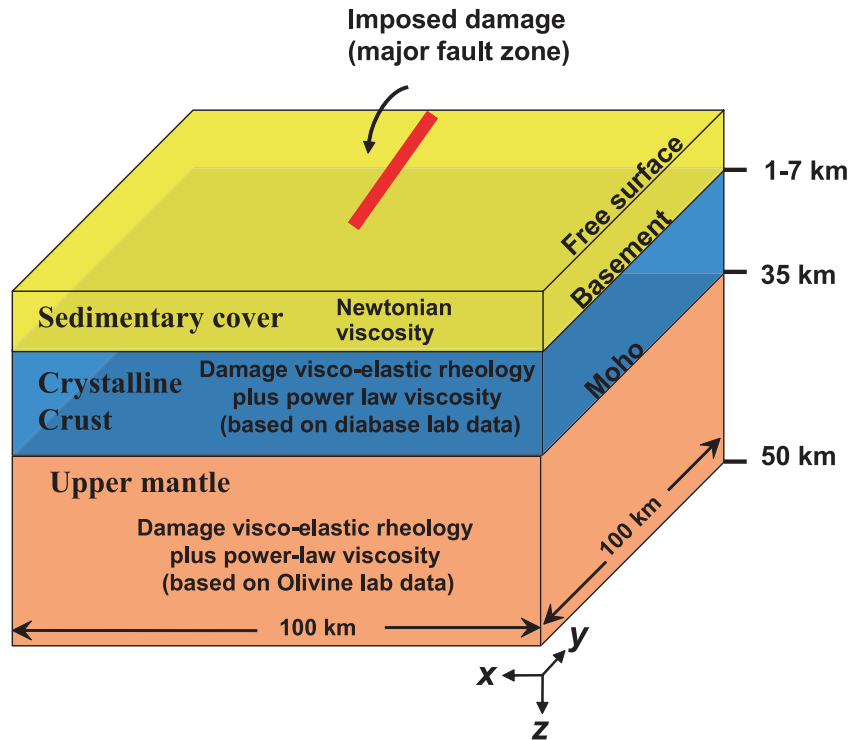

Figure 2. A schematic diagram of the 3-D lithospheric structure used in the numerical simulations along with a given temperature gradient. The thickness of the upper sedimentary cover varies from 1 to 7 km in different model realizations. The imposed main shock damage zone extends from the free surface to a depth of 15 km. See text for additional explanations.
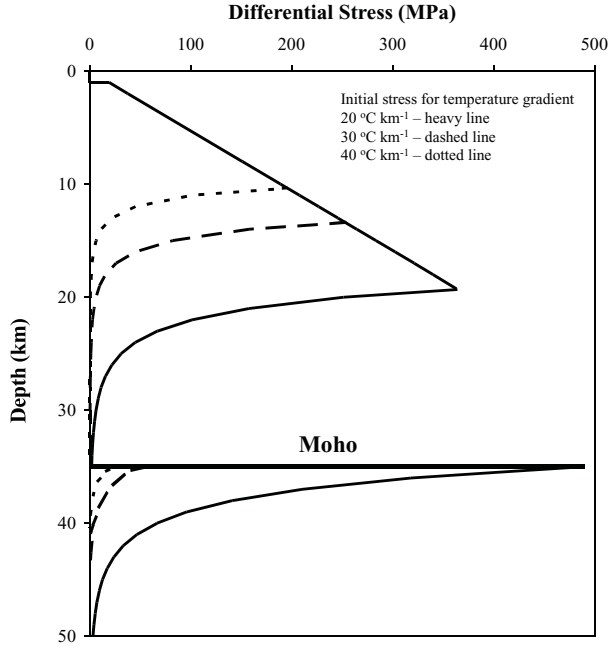
Differential Stress (MPa)

Figure 3. Regional tectonic stress fields versus depth for a constant strain rate of 10^{-15} s^{-1} and different temperature gradients indicated in the legend. The small step in the uppermost part of the curve corresponds to the interface between the weak sedimentary cover and the underlying crystalline crust.

and initial Poisson's ratio of the top sedimentary layer are $\rho^{\mathrm{SED}} = 2400$ kg m^{-3}, $\mu_0^{\mathrm{SED}} = 2 \times 10^{10}$ Pa and $\nu_0^{\mathrm{SED}} = 0.2$. The corresponding parameters for the crust and upper mantle layers are $\rho^C = 2800$ kg m^{-3}, $\mu_0^C = 6 \times 10^{10}$ Pa, $\nu_0^C = 0.2$; $\rho^{\mathrm{UM}} = 3200$ kg m^{-3}, $\mu_0^{\mathrm{UM}} = 12 \times 10^{10}$ Pa, $\nu_0^{\mathrm{UM}} = 0.2$.

The total strain tensor ε_{ij}^t in each layer is written as a sum of three strain components associated with different deformation mechanisms

$$\varepsilon_{ij}^t = \varepsilon_{ij}^e + \varepsilon_{ij}^i + \varepsilon_{ij}^d, \tag{20}$$

where ε_{ij}^e is elastic strain related to the stress tensor through (5), ε_{ij}^i denotes the damage-related inelastic strain with accumulation rate $e_{ij} = d\varepsilon_{ij}^i/dt$ calculated using eq. (8), and ε_{ij}^d represents ductile strain. As discussed below, the latter may be generated by a variety of mechanisms including dislocation creep, solid state diffusion, and solution–diffusion–precipitation processes (e.g. Kohlstedt *et al.* 1995). The superposition in eq. (20) of strain tensors associated with different deformation mechanisms is an expansion of the classical Maxwell viscoelastic model. A similar superposition was used recently by Regenauer-Lieb & Yuen (2003) to model the rheology of the crust and upper mantle.

The rate of the ductile strain accumulation in the sedimentary layer is calculated using Newtonian viscosity

$$\dot{\varepsilon}_{ij}^d = \frac{1}{\eta}\tau_{ij}, \tag{21}$$

with a relatively low viscosity $\eta = 10^{20}$ Pa s. The ductile flow in the crystalline crust and upper mantle can be described by empirical constitutive relations that express the rate of ductile strain accumulation as a function of stress and temperature for the dominant lithologies of continental lithosphere (e.g. Goetze 1978; Brace & Kohlstedt 1980; Kirby 1983; Kohlstedt *et al.* 1995; Ranalli 1995). The common lithologies of the continental lithosphere are quartz–

diorite (upper crust), diabase (lower crust) and dunite/olivine (mantle). Most of the experimental constitutive relations are established for minerals, assuming that the weakest dominant minerals control the flow rate of the rock (e.g. Brace & Kohlstedt 1980). Direct observations of ductile shear zones and indirect analyses of seismic anisotropy in mantle rocks demonstrate that dislocation creep dominates at stresses above 10 MPa (e.g. Karato 1989). A power-law rheology is widely accepted for expressing the strain rate of the dislocation flow (e.g. Weertman 1978)

$$\dot{\varepsilon}_{ij}^d = A\sigma^{n-1} \exp\left(-\frac{Q + PV^*}{R_g \cdot T}\right)\tau_{ij}, \tag{22}$$

where A and n are empirical constants, τ_{ij} is the deviatoric stress component, σ is the amplitude of τ_{ij}, Q is activation energy, V^* is activation volume, P is pressure, T is temperature, and the gas constant $R_g = 8.314$ J mol^{-1} $^\circ$K. The material constants for the creep law of the diabase, which controls the ductile flow of the lower continental crust, are $A = 6.31 \times 10^{-20}$ Pa^{-n} s^{-1}, $n = 3.05$, and $Q = 276$ kJ mol^{-1} (Carter & Tsenn 1987). The ductile flow in the mantle is controlled by the olivine/dunite with material constants $A = 7 \times 10^{-14}$ Pa^{-n} s^{-1}, $n = 3$, and $Q = 520$ kJ mol^{-1} (Kirby & Kronenberg 1987). The differences in reported activation volume $V^* = 5 \times 10^{-6}$ to 27×10^{-6} m^3 mol^{-1} (Hirth & Kohlstedt 2003) multiplied by pressure values corresponding to depths of several hundred kilometres produce an uncertainty of several orders of magnitude for the viscosity. However, for relatively low pressures corresponding to depths less than 100 km, the PV^* term in (22) is negligible.

The initial stress field in the 3-D model is given by the sum of a depth-dependent regional stress and a co-seismic stress distribution corresponding to an imposed strong earthquake. The co-seismic stress components are calculated using the Okada (1992) code. The regional stress follows a yielding stress envelope given by the intersection of brittle and ductile regimes (Fig. 3) for a strain rate of 10^{-15} s^{-1} and temperature gradients of 20, 30 and 40°C km^{-1} in different model realizations. The transition depth from brittle deformation to ductile flow in the crust occurs at a temperature of about 300°C (Brace & Kohlstedt 1980; Tsenn & Carter 1987). The initial stress in the brittle seismogenic zone is calculated using an internal friction angle of 35°, corresponding to $\xi_0 = -0.8$ in (7).

The superposition of the above regional and co-seismic stress fields in a model configuration with fixed boundaries is followed by internal stress relaxation, during a process associated with damage increase and gradual inelastic strain in the seismogenic zone, and ductile flow in the underlying substrate. When the damage reaches a critical value α_c associated with loss of the convexity of the strain energy function (3), the quasi-static solution for damage accumulation becomes unstable and dynamic stress drop occurs. The dynamic stress drop (not analysed in detail here) produces a reduction of the elastic strain in a rapid process during which the shear modulus remains very low. The brittle failure leads to an abrupt increase of plastic deformation that corresponds to slip in simpler models with planar faults. Similarly to our previous works on coupled evolution of earthquakes and faults (Ben-Zion *et al.* 1999; Lyakhovsky *et al.* 2001a; Ben-Zion & Lyakhovsky 2002), we assume that during brittle failure the deviatoric stress drops locally to zero leaving only the volumetric component. After the failure, the local stress conditions favour healing according to eq. (7) and the depth-dependent lithostatic pressure. The elastic stress can then increase due to stress transfers until it reaches again the critical level for brittle instability.

A brittle failure at any fault location may lead to rupture propagation. This is simulated with a quasi-dynamic procedure (Lyakhovsky *et al.* 2001a) using iterative stress transfer calculations and

incorporation of dynamic weakening. As discussed in the appendix, the latter is associated with a reduction of the critical value of the damage variable at all elements of the model during the rupture process to a dynamic level α_d given by

$$\alpha_d = \alpha_c - \sqrt{\tau_r \frac{d\alpha}{dt}}, \qquad (23)$$

where τ_r is a material property controlling the weakening during the rupture propagation. When the rupture stops propagating, the damage failure threshold reverts everywhere to the static value α_c. The increments of co-seismic plastic strain ε_{ij}^p in the elements that failed during the rupture process are integrated to calculate the seismic potency tensor (Ben-Zion 2003) of the event, $P_{ij} = \int_V \varepsilon_{ij}^p dV$. The corresponding earthquake magnitude M is calculated from the empirical potency-magnitude scaling relation of Ben-Zion & Zhu (2002)

$$\log_{10} P_0 = 0.06M^2 + 0.98M - 4.87, \qquad (24)$$

where $P_0 = \sqrt{2P_{ij}P_{ij}}$ is in km^2 cm.

4.2 Aftershock statistics in 3-D numerical simulations

We first consider cases designed to study the decay rates, frequency-size statistics and depth extent of aftershock sequences. The minimum and maximum sizes of the simulated events are governed by the size of the numerical elements, the large scale dimensions of the seismogenic zone and other lithospheric layers, the size of the imposed main shock, and rheological parameters. To have a reasonable range of event sizes during a practical computation time, we use together with the large scale dimensions discussed in Section 4.1, numerical elements in the seismogenic zone with size of about 500 m and an imposed main shock that extends in the *y*-direction beyond the model configuration of Fig. 2. All cases below start with an imposed main shock having a 5 m of slip over a fault zone centred at $x = 50$ km and extending over the range $50 \leq y \leq 150$ km, $0 \leq z \leq 15$ km. The magnitude of the imposed main shock is $M = 7.3$ and each run produces seismic activity for one year following the main shock. The key rheological parameter that affects the maximum size of the simulated events is the dynamic weakening timescale τ_r of (23), while the key parameter that affects the other properties of the aftershock sequences is the ratio R. In this section we use a fixed $\tau_r = 300$ s and analyse the dependency of the results on the parameter R, as well as the lithospheric structure and thermal regime. In the next section we consider results associated with different values of τ_r. In all simulations we use the following lab-based damage parameters: $\xi_0 = -0.8$, $C_d = 10$ s^{-1}, $C_1 = 10^{-5}$ s^{-1} and $C_2 = 0.05$. The parameter C_v varies among cases to produce in the crystalline crust different values of the material parameter $R = \mu_0 \cdot C_v$ with $\mu_0 = 6 \times 10^{10}$ Pa.

Figs 4(a)–(e) show the number of model aftershocks for R values varying from 0.1 to 10, a thickness of the weak sedimentary cover of 1 km, and a temperature gradient of 20°C km^{-1}. In each case, the daily seismicity rate during 100 days after the main shock was fitted with the least-squares method to the modified Omori law (eq. 1). In agreement with the 1-D analytical results of Section 3, the duration and event productivity of the simulated aftershock sequences decrease with increasing R values. If R is small, the damage-related inelastic strain is very small and the parameters of the aftershock statistics depend only weakly on the R value. Thus the simulated sequences with $R = 0.1$ and $R = 1$ (Figs 4a and b) can be fitted by the modified Omori law with p values that change only from 0.8 to 0.9. A further increase of R
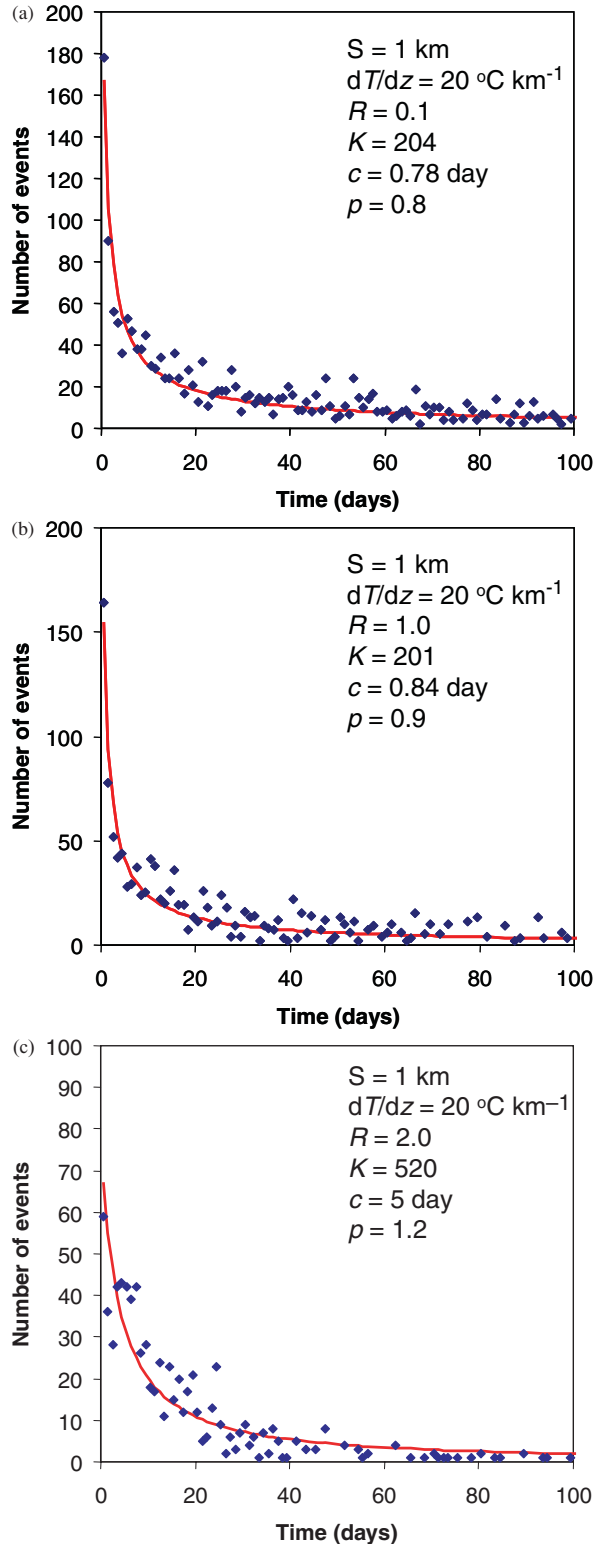

Figure 4. (a) Daily rates of aftershocks in a 3-D numerical simulation with model realization having $R = 0.1$, sedimentary cover of 1 km, and temperature gradient of 20°C km^{-1}. The line gives least-squares fit to the data points based on the modified Omori law with parameters given in the legend. (b) Same as (a) for $R = 1.0$. (c) Same as (a) for $R = 2.0$. (d) Same as (a) for $R = 3.0$. (e) Same as (a) for $R = 10.0$.
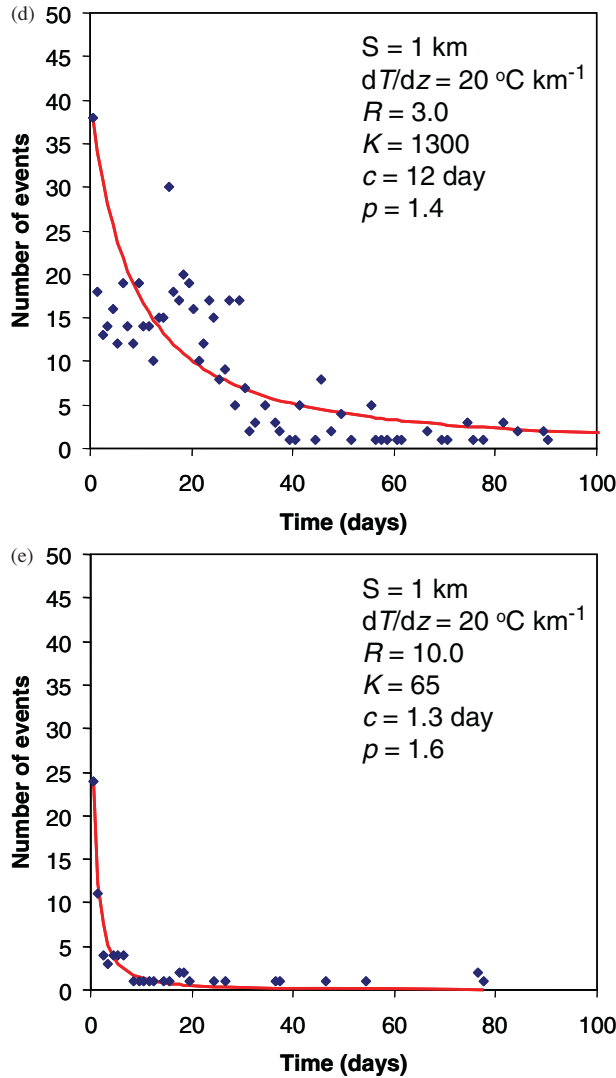
Figure 5. Cumulative frequency-size statistics of aftershocks in 3-D simulations with different R values. The thickness of the sedimentary layer is 1 km and the temperature gradient is $20°C$ km^{-1}.

Figure 4. (*Continued.*)

above 1, however, affects significantly the aftershock sequence. For $R = 2$ and $R = 3$, the simulated sequences (Figs 4c and d) are fitted with p values that are equal to 1.2 and 1.4, respectively. In addition, the number of simulated earthquakes decreases significantly with increasing R value, leading to lower quality of the fitting parameters. For $R = 10$, only a few tens of earthquakes occur in the first week following the main shock, and after 2 weeks the activity becomes negligibly small. This sequence can also be fitted by the modified Omori law (with $p = 1.6$), but the quality of the fitting is poor.

The cumulative frequency-size statistics of aftershocks generated by model realizations with $R = 0.1$ and $R = 1$ follow the Gutenberg–Richter relation (2a) over about 3 orders of magnitudes with b values of about 0.7 (Fig. 5). Model realizations with higher values of R produce aftershocks over a magnitude range that becomes increasingly narrower with increasing R and cannot be described by power-law statistics. The shortening of aftershock sequences with increasing R values (Fig. 4), accompanied by the narrowing range of event sizes and changes in the frequency-size statistics (Fig. 5), suggest that model simulations with $R > 5$ of evolving seismicity with multiple
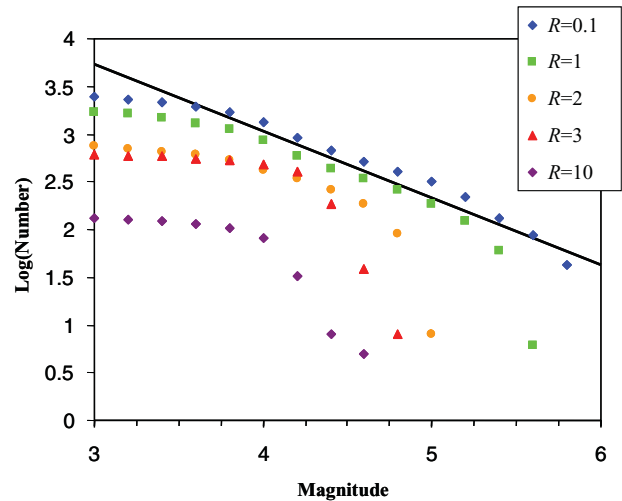
main shocks would produce a swarm-type activity rather than clear main shock and aftershock sequences.

Figs 6 and 7 illustrate the sensitivity of the aftershocks decay rate to the lithospheric structure and thermal regime. The events number and duration of the aftershock sequences decrease significantly with increasing thickness of the weak sedimentary cover, from 1 km (Fig. 4b) to 4 km (Fig. 6a) and to 7 km (Fig. 6b). All model parameters in those three cases other than the thickness of the sedimentary layer are the same. The fitted p values increase with increasing thickness of sediments, in agreement with the decreasing duration and productivity of the aftershock sequences. The direct effect of the temperature gradient on temporal properties of the aftershocks is relatively weak. Fig. 7 shows results of simulations with initial regional stress distributions calculated using yielding stress envelopes (Fig. 3) for a strain rate of 10^{-15} 1/s and temperature gradients of 30 and $40°C$ km^{-1}. The other model parameters are the same as in Fig. 4b, which is generated with corresponding initial stress associated with $20°C$ km^{-1}. The number of aftershocks decreases with increasing temperature gradient, but the duration of the aftershock sequences remains about the same and the corresponding p value increases only slightly (compare Fig. 4b with Figs 7a and b).

On the other hand, the temperature gradient affects strongly, along with the employed R value, the depth distribution of the aftershock hypocentres (i.e. the thickness of the seismogenic zone). The depth of the brittle–ductile transition in the crystalline crust, or the bottom boundary of the seismogenic zone, is controlled by the temperature gradient and the strain rate. In a model with $R = 0.1$ and temperature gradient of $20°C$ km^{-1}, the hypocentres of the simulated aftershocks are concentrated in the top 15 km (Fig. 8a). The maximum hypocentre depth decreases with time from the main shock and the depth of the early hypocentres extends below 35 km. The temporal evolution of the maximum hypocentre depth reflects a transient deepening of the brittle–ductile transition depth, which is generated by the high strain rates produced by the main shock. A similar temporal evolution is produced in milder forms by a model realization with $R = 1.0$ and temperature gradient of $20°C$ km^{-1} (Fig. 8b), and a model with $R = 1.0$ and temperature gradient of $30°C$ km^{-1} (Fig. 8c). In these cases, most simulated hypocentres are concentrated in the top 5–10 km of the crust.
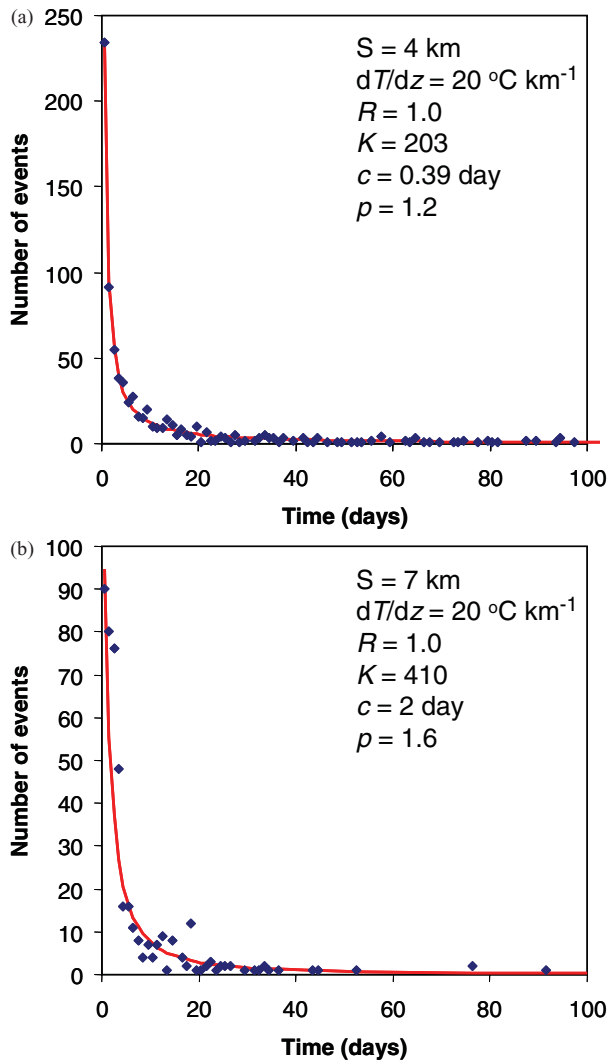
Figure 6. (a) Daily rates of aftershocks in a 3-D model realization having a weak sedimentary cover of 4 km, $R = 1.0$, and temperature gradient of $20°C$ km^{-1}. The line gives least-squares fit to the data points based on the modified Omori law with parameters given in the legend. (b) Same as (a) with a weak sedimentary cover of 7 km.

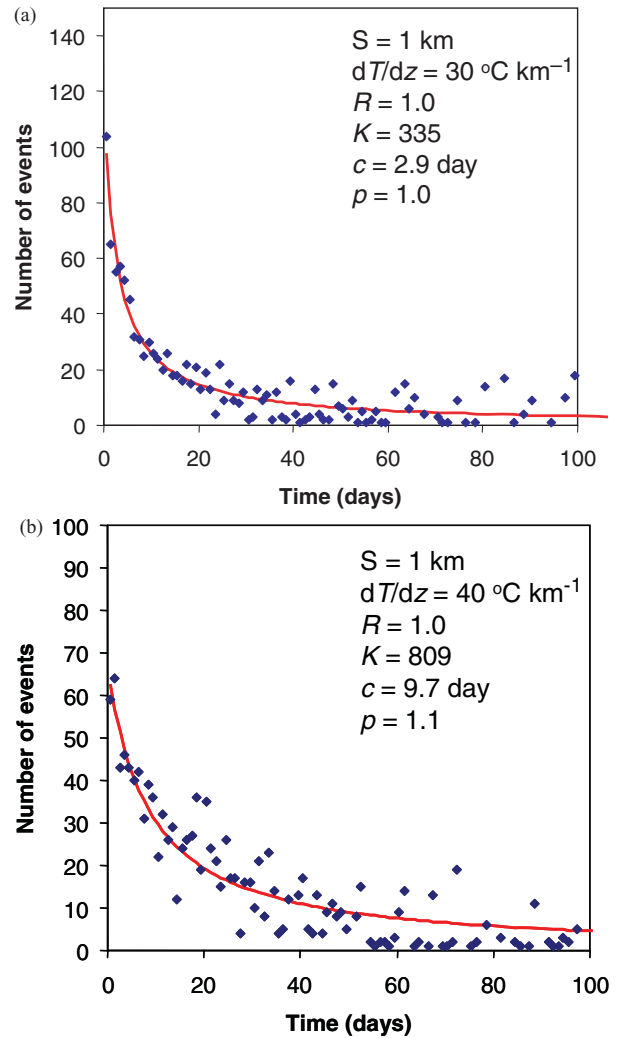**Figure 7.** (a) Daily rates of aftershocks in a 3-D model realization having a temperature gradient of $30°C$ km^{-1}, $R = 1.0$, and weak sedimentary cover of 1 km. The line gives least-squares fit to the data points based on the modified Omori law with parameters given in the legend. (b) Same as (a) with a temperature gradient of $40°C$ km^{-1}.

4.3 Largest aftershocks in 3-D numerical simulations

As mentioned in the previous section, the maximum size of the simulated events depends (in addition to geometrical parameters) on the dynamic weakening timescale τ_r of (23). In this section we examine the magnitudes of the largest simulated aftershocks in cases with various imposed source sizes and various values of τ_r. We consider a set of simulations with the imposed $M = 7.3$ main shock of the previous section, and additional two sets with imposed main shock magnitudes of $M = 6.8$ and $M = 6.5$. The latter two cases have the same source dimensions as in the previous section, but imposed slip values of 0.5 and 0.1 m. These correspond to a reduction of the potency value from that associated with the $M = 7.3$ main shock by factors of 10 and 50, respectively. In each set of simulations with a given imposed main shock size, the dynamic weakening timescale is varied by several orders of magnitudes. All the other parameters are kept fixed. The thickness of the weak sedimentary cover is 1 km, the thermal gradient is $20°C$ km^{-1}, and the R value is 1.

As indicated by eq. (23) for the dynamic weakening, the critical damage value decreases proportionally to the square root of τ_r. The number of elements involved in a seismic event, and hence the potency value P_0 of the event, should increase with the same scaling. Since the magnitude is approximately proportional to log (P_0) for a narrow magnitude range, the strongest simulated magnitudes should be proportional to log (τ_r). This is seen in Fig. 9, where we plot the largest simulated magnitudes versus τ_r in a log scale for all three simulation sets. The aftershock magnitudes of the second set with the imposed $M = 6.8$ main shock follow closely the expected log-linear relation (solid line in Fig. 9) for the entire range of employed τ_r values. The dashed line associated with the imposed $M = 7.3$ main shock is shifted up by 0.5 magnitude units from the solid line, and the dotted line associated with the imposed $M = 6.5$ main shock is shifted down by 0.3 units. In the set with main shock magnitude $M = 7.3$, the largest simulated aftershocks are close to the expected log-linear line for $\tau_r \leq 300$, and fall below it for larger values of τ_r. The latter is a finite size effect associated

(a) R = 0.1, dT/dz = 20 °C km⁻¹

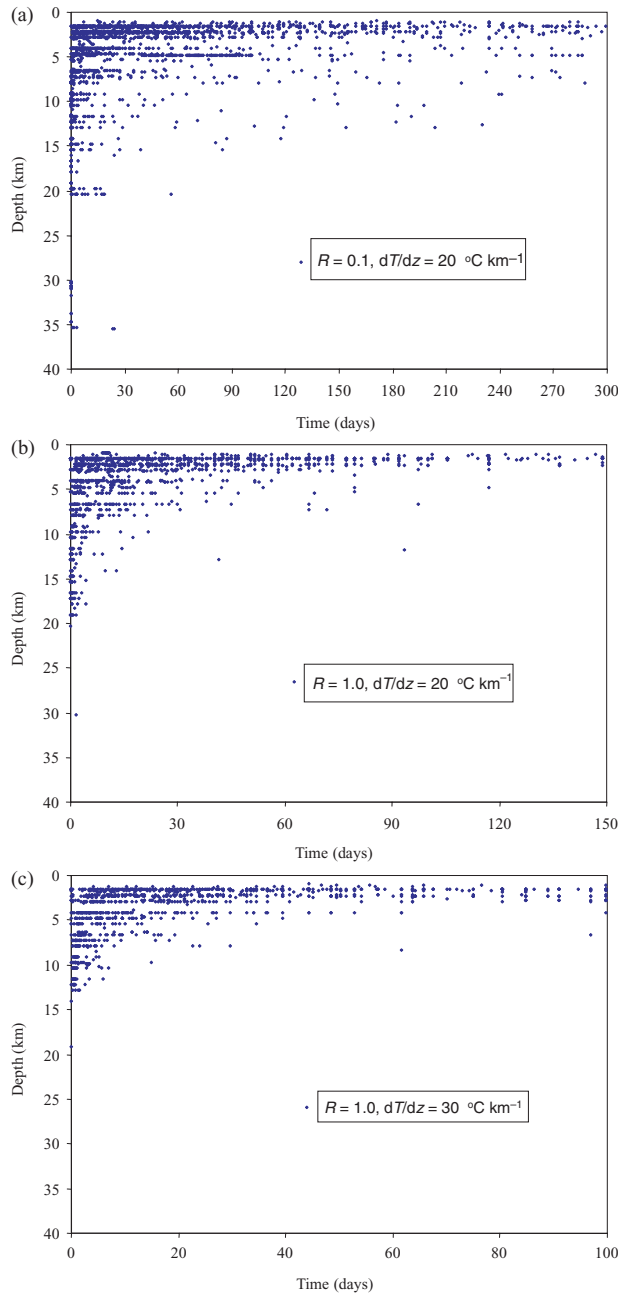(b) R = 1.0, dT/dz = 20 °C km⁻¹

(c) R = 1.0, dT/dz = 30 °C km⁻¹

Figure 8. (a) Depth of aftershock hypocentres in a 3-D model realization having $R = 0.1$, sedimentary cover of 1 km, and temperature gradient of $20°C$ km^{-1}. (b) Same as (a) with $R = 1.0$. (c) Same as (b) with temperature gradient of $30°C$ km^{-1}.
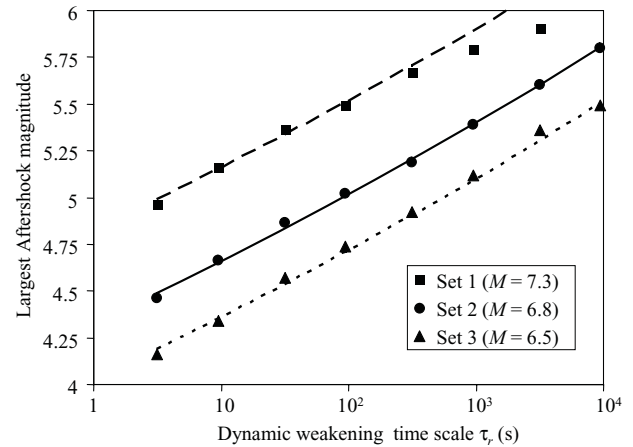

Figure 9. Magnitudes of the largest aftershocks in 3-D model simulations with different imposed main shock size (indicated in the legend) as a function of the dynamic weakening timescale. See text for additional explanations.

5 DISCUSSION

We used a 1-D version of a continuum-based damage rheology model (Lyakhovsky *et al.* 1997a; Hamiel *et al.* 2004) to derive analytical results for aftershock decay rates under a constant strain boundary condition. The general analytical solution (eq. 16a) is an exponential function that depends on the material parameter $R = \mu_0 \cdot C_v$, associated with the ratio of timescale for brittle damage accumulation to timescale for viscous relaxation, and on the initial damage and a threshold strain level for material degradation. For some simplifying conditions, we obtain a solution in the form of the modified Omori power law with an analytical exponent $p = 1$. The assumed constant strain boundary condition is appropriate for a relatively short time interval (e.g. one year) following the occurrence of large earthquakes, which produce abrupt strain steps leading to a relaxation process in the surrounding medium. In contrast, the time interval leading to the occurrence of large seismic events should be modelled with a constant stress boundary condition, which produces an unstable process leading to a system size event. Ben-Zion & Lyakhovsky (2002) showed that a simplified version of the damage rheology model (without inelastic viscous deformation prior to brittle instabilities) leads under constant stress boundary condition to accelerated seismic release culminated by a system size event (see also Turcotte *et al.* 2003). The analytical results were augmented by 3-D numerical simulations for various cases of R, thickness of a weak sedimentary cover, temperature gradient, and dynamic weakening value.

The material parameter R is the major factor controlling the decay rate, duration and frequency-size statistics of aftershocks, as well as the partition of the stored elastic strain energy between seismic and aseismic components of deformation. The fraction χ of the energy released in brittle deformation is referred to as the degree of seismic coupling. (We note that this should not be confused with the 'seismic efficiency' denoting (e.g. Ben-Zion 2003) the ratio between the radiated seismic energy and the total strain energy release during an earthquake rupture.) The parameter χ is inversely proportional to the material parameter R. This can be shown analytically for the 1-D version of our damage rheology (Section 3) representing uniform deformation. In this case, the seismic deformation in a process associated with evolution of the damage state variable α from 0 to 1 can be estimated from the reduction of the elastic modulus

with the fact that for high τ_r values the size of the largest simulated aftershock approaches the model dimension. The results of the simulation set with main shock magnitude $M = 6.5$ fit well (as the set with $M = 6.8$) the expected log-linear relation over the entire range of the employed τ_r values. The line fits of Fig. 9 indicate that values of the dynamic weakening timescale τ_r in the range $3 \times 10^2 - 3 \times 10^4$ s produce typical observed ΔM values of the Båth law. For example, a value of $\Delta M = 1.2$ is associated with τ_r of about 1000 s.

(see eq. 9) as

$$2\mu_0 \varepsilon_{\text{seismic}} = \sigma. \tag{25}$$

The rate of aseismic deformation can be estimated from the rate of inelastic strain accumulation (see eq. 11) as

$$d\varepsilon_i/dt = \dot{\alpha} C_v \sigma/2. \tag{26a}$$

Integrating (26a) over time, the aseismic strain during a deformation cycle is given by

$$\varepsilon_{\text{aseismic}} = C_v \sigma/2. \tag{26b}$$

From eqs (25) and (26b), the ratio of the aseismic to seismic components of deformation is

$$\varepsilon_{\text{aseismic}}/\varepsilon_{\text{seismic}} = \mu_0 \cdot C_v \equiv R. \tag{27}$$

The fraction of elastic strain released during a seismic cycle as brittle deformation can be estimated from eq. (27) as

$$\chi = \varepsilon_{\text{seismic}}/(\varepsilon_{\text{aseismic}} + \varepsilon_{\text{seismic}}) = 1/(1 + R). \tag{28}$$

It is thus seen that the values $R = 0.1$, 1 and 10 that were used in Sections 3 and 4 correspond, respectively, to $\chi = 0.9$, 0.5 and 0.09. The above results open the possibility of estimating the ratio between seismic and aseismic components of deformation in a region from analysis of the R value that best characterizes observed properties (decay rate, duration, productivity and frequency-size statistics) of aftershock sequences in the region.

The general analytical solution (16a) for aftershock rates is associated with an exponential function. However, the analytical results and numerical simulations for various values of R can be fitted well by the modified Omori power-law relation. This illustrates the difficulty of deriving reliable information on functional forms and parameter values from aftershock data. Vere-Jones *et al.* (2001) and Ben-Zion & Lyakhovsky (2002) made a similar point in relation to fitting data associated with accelerated seismic release before large earthquakes. The non-uniqueness of fitting earthquake observations has been discussed in many other theoretical and observational works. Gross & Kisslinger (1994) and Kisslinger (1996) demonstrated with several aftershock sequences that expressions associated with a stretched exponential function can fit aftershock decay rates as well as the modified Omori law. Narteau *et al.* (2002) showed the same using sums of exponentials. Scholz (1968) and Hirata (1987) used exponential functions to fit acoustic emission data in rock fracture experiments. Benioff (1951) derived a solution with logarithmic and exponential functions for strain energy release, based on creep rheology, and used it to fit (cumulative Benioff strain) data of several California aftershock sequences.

Our analytical and numerical results indicate that the primary controlling factor on several properties of aftershock sequences is the value of the material parameter R, which is inversely proportional to the degree of seismic coupling across a fault. R values of about one or lower, corresponding to high-viscosity material, produce clear aftershock sequences with decay rates that can be fitted by the modified Omori law with $p \sim 1$. The frequency-size statistics of such aftershock sequences follow the Gutenberg–Richter power-law relation with b values of about 0.7, compatible with the $b = 0.75$ global average for shallow strike slip earthquakes (Frohlich & Davis 1993). On the other hand, R values of about three or larger, corresponding to low-viscosity material, produce diffuse aftershock sequences with higher effective p values, shorter duration and smaller number of events. The frequency-size statistics of these sequences are peaked and cannot be described by the Gutenberg–Richter relation. Simulations with multiple main shocks and $R > 5$ are expected to

produce a swarm-like behaviour. The results provide a simple explanation for the fact that regions with high heat flow and/or high fluid activity (like volcanic domains and oceanic transform faults) have swarms and diffuse earthquake patterns, while continental regions with low heat flow have clear long aftershock sequences (e.g. Mogi 1967; Kisslinger & Jones 1991; Utsu *et al.* 1995; McGuire *et al.* 2005).

Additional important structural and geophysical parameters are the thickness of a weak sedimentary cover and the thermal gradient. Regions with a sedimentary layer that is thicker than a few km produce weaker aftershock sequences, with a smaller number of events and faster decay, similar to what is produced by high R values. Increasing the temperature gradient leads to a smaller number of events, but the aftershock decay rate and duration remain largely unaffected. Thus the temperature gradient does not have a strong direct effect on properties of aftershock sequences, although it can have a major indirect effect through the R value. However, increasing temperature gradient reduces the overall depth extent of the brittle seismogenic zone and the simulated aftershocks. In addition, the maximum hypocentre depth decreases with time from the main shock due to a transient deepening of the brittle–ductile transition depth produced by the high strain rates generated by the main shock. These results are compatible with observed correlations between the depth of seismicity and temperature gradient (Magistrale 2002), and temporal evolution of the depth of aftershocks following the 1992 Landers CA earthquake (Rolandone *et al.* 2004).

The results of this work are associated with aftershock sequences of single main shocks with zero background seismicity. Additional related cases can be obtained by adding to the results a constant value representing the ongoing background seismicity. In a more general study, the main shocks should be generated spontaneously by the gradual remote loading, as an integral part of the evolving seismicity, rather than being imposed. This will be the subject of a continuing work. Our analysis indicates that properties of aftershocks are sensitive to a number of geological and physical parameters. The relations between aftershock properties, the temperature field, and degree of seismic coupling have been examined in a number of observational studies. In contrast, the relations between aftershock properties and sedimentary cover layers received little attention. This should be the subject of future observational works.

REFERENCES

Agnon, A. & Lyakhovsky, V., 1995. Damage distribution and localization during dyke intrusion, in *The Physics and Chemistry of Dykes,* pp. 65–78, eds Baer, G. & Heimann A., Balkema, Brookfield, Massachusetts.

Båth, M., 1965. Lateral inhomogeneities in the upper mantle. *Tectonophysics,* **2,** 483–514.

Benioff, H., 1951. Earthquakes and rock creep (Part I: creep characteristics of rocks and the origin of aftershocks), *Bull. seism. Soc. Am.,* **41,** 31–62.

Ben-Zion, Y., 2003. Appendix 2. Key Formulas in Earthquake Seismology, in *International Handbook of Earthquake and Engineering Seismology,* pp. 1857–1875, eds Lee, W.H.K., Kanamori, H., Jennings, P.C. & Kisslinger, C., Part B, Academic Press.

Ben-Zion, Y. & Lyakhovsky, V., 2002. Accelerating seismic release and related aspects of seismicity patterns on earthquake faults, *Pure appl. Geophys.,* **159,** 2385–2412.

Ben-Zion, Y. & Zhu, L., 2002. Potency-magnitude scaling relations for Southern California earthquakes with $1.0 < M_L < 7.0$, *Geophys. J. Int.,* **148,** F1–F5.

Ben-Zion, Y., Dahmen, K., Lyakhovsky, V., Ertas, D. & Agnon, A., 1999. Self-driven mode switching of earthquake activity on a fault system, *Earth planet. Sci. Lett.,* **172,** 11–21.

Boettcher, M.S. & Jordan, T.H., 2004. Earthquake scaling relations for mid-ocean ridge transform faults, *J. geophys. Res.,* **109,** doi:10.1029/2004JB003110.

Brace, W.F. & Kohlstedt, D.L., 1980. Limits on lithospheric stress imposed by laboratory experiments, *J. geophys. Res.,* **85,** 6248–6252.

Budiansky, B. & O'Connell, R.J., 1976. Elastic moduli of a cracked solid, *Int. J. Solids Struct.,* **12,** 81–97.

Carter, N.L. & Tsenn, M.C., 1987. Flow properties of continental lithosphere, *Tectonophysics,* **136,** 27–63.

Cole, J.D., 1968. *Perturbation Method in Applied Mathematics,* Blaisdell Pub. Co.

Cundall, P.A., 1989. Numerical experiments on localization in frictional materials, *Ign. Arch.,* **59,** 148–159.

Cundall, P.A. & Board, M., 1988. A microcomputer program for modeling large-strain plasticity problems, in *Numerical Methods in Geomechanics,* pp. 2101–2108, ed. Swoboda, C., Proc. 6th Int. Conf. Numerical Methods in Geomechanics, Innsbruck, Balkema, Rotterdam.

Das, S. & Scholz, C.H., 1981. Theory of time-dependent rupture in the earth, *J. geophys. Res.,* **86,** 6039–6051.

Davis, S.D. & Frohlich, C., 1991. Single-link cluster analysis of earthquake aftershocks: decay laws and regional variations, *J. geophys. Res.,* **96,** 6335–6350.

Dieterich, J.H., 1994. A constitutive law for rate of earthquake production and its application to earthquake clustering, *J. geophys. Res.,* **99,** 2601–2618.

Ekland, I. & Temam, R., 1976. *Convex Analysis and Variational Problems,* Elsevier, Amsterdam.

Frohlich, C. & Davis, S.D., 1993. Teleseismic *b* values; or, much ado about 1.0, *JGR,* **98,** 631–644.

Goetze, C., 1978. The mechanisms of creep in olivine, *Phil. Trans. R. Soc. Lond. A,* **288,** 99–119.

Gross, S.J. & Kisslinger, C., 1994. Tests of models of aftershock rate decay, *Bull. seism. Soc. Am.,* **84,** 1571–1579.

Hamiel, Y., Liu, Y., Lyakhovsky, V., Ben-Zion, Y. & Lockner, D., 2004. A Visco-elastic damage model with applications to stable and unstable fracturing, *Geophys. J. Int.,* **159,** 1155–1165, doi: 10.1111/j.1365-246X.2004.02452.x.

Hirth, G. & Kohlstedt, D.L., 2003. Rheology of the upper mantle and the mantle wedge: a view from the experimentalists, in *Inside the Subduction Factory,* Vol. 138, pp. 83–105, ed. Eiler, J., American Geophysical Union, Monograph.

Hirata, T., 1987. Omori's power law aftershock sequences of microfracturing in rock fracture experiments, *J. geophys. Res.,* **92,** 6215–6221.

Jaeger, J.C. & Cook, N.G.W., 1976. *Fundamentals of Rock Mechanics,* Chapman and Hall, New York.

Kachanov, L.M., 1986. *Introduction to continuum damage mechanics,* p. 135, Martinus Nijhoff Publishers.

Karato, S.-I., 1989. Seismic anisotropy: mechanisms and tectonic implications, in *Rheology of Solids and of the Earth,* pp. 393–422, eds Karato, S.-I. & Toriumi, M., Oxford Univ. Press, New York.

Kirby, S.H., 1983. Rheology of the lithosphere, *Rev. Geophys.,* **21,** 1458–1487.

Kirby, S.H. & Kronenberg, A.K., 1987. Rheology of the lithosphere: selected topics, *Rev. Geophys.,* **25,** 1219–1244.

Kisslinger, C., 1996. Aftershocks and fault-zone properties, *Advances in Geophysics,* **38,** 1–36.

Kisslinger, C. & Jones, L.M., 1991. Properties of aftershock sequences in southern California, *J. geophys. Res.,* **96,** 11 947–11 958.

Kohlstedt, D.L., Evans, B. & Mackwell, S.J., 1995. Strength of the lithosphere: constraints imposed by laboratory experiments, *J. geophys. Res.,* **100,** 17 587–17 602.

Krajcinovic, D., 1996. *Damage Mechanics,* Elsevier, Amsterdam.

Lyakhovsky, V., Podladchikov, Y. & Poliakov, A., 1993. Rheological model of a fractured solid, *Tectonophysics,* **226,** 187–198.

Lyakhovsky, V., Ben-Zion, Y. & Agnon, A., 1997a. Distributed damage, faulting and friction, *J. geophys. Res.,* **102,** 27 635–27 649.

Lyakhovsky, V., Reches, Z., Weinberger, R. & Scott, T.E., 1997b. Non-linear elastic behavior of damaged rocks, *Geophys. J. Int.,* **130,** 157–166.

Lyakhovsky, V., Ben-Zion, Y. & Agnon, A., 2001a. Earthquake cycle, fault zones and seismicity patterns in a rheologically layered lithosphere, *J. geophys. Res.,* **106,** 4103–4120.

Lyakhovsky, V., Ilchev, A. & Agnon, A., 2001b. Modeling of damage and instabilities of rock mass by means of a non-linear rheological model, in *Dynamic rock mass response to mining,* pp. 413–420, eds van Aswegen, G., Durrheim, R.J. & Ortlepp, W.D., Rockbursts and seismicity in mines—RaSiM5, South African Institute of Mining and Metallurgy, Johannesburg, South Africa.

Lyakhovsky, V., Ben-Zion, Y. & Agnon, A., 2005. A visco-elastic damage rheology and rate- and state-dependent friction, *Geophys. J. Int.,* **161,** 179–190, doi: 10.1111/j.1365-246X.2005.02583.x.

Magistrale, H., 2002. Relative contributions of crustal temperature and composition to controlling the depth of earthquakes in southern California, *Geophys. Res. Lett.,* **29**(10), 1447, doi:10.1029/2001GL014375.

McGuire, J.J., Boettcher, M.S. & Jordan, T.H., 2005. Foreshock sequences and short-term earthquake predictability on East Pacific Rise Transform Faults, *Nature,* **434,** 457–461.

Mogi, K., 1967. Earthquakes and fractures, *Tectonophysics,* **5,** 35–55.

Narteau, C., Shebalin, P. & Holschneider, M., 2002. Temporal limits of the power law aftershock decay rate, *J. geophys. Res.,* **107,** Art. No. 2359.

Newman, W.I. & Phoenix, S.L., 2001. Time-dependent fiber bundles with local load sharing, *Physical Rev. E.,* **63,** 021507.

Nur, A. & Booker, J.R., 1972. Aftershocks caused by pore fluid flow?, *Science,* **175,** 885—887.

Okada, Y., 1992. Internal deformation due to shear and tensile faults in a half-space, *Bull. seism. Soc. Am.,* **82,** 1018–1040.

Peng, Z. & Ben-Zion, Y., 2006. Temporal changes of shallow seismic velocity around the Karadere-Duzce branch of the north Anatolian fault and strong ground motion, *Pure appl. Geophys.,* **163,** 567–599, doi: 10.1007/s00024-005-0034-6.

Peng, Z., Vidale, J.E., Ishii, M. & Helmstetter, A., 2006. Seismicity rates immediately before and after main shock rupture from high-frequency waveforms in Japan, *J. geophys. Res.,* in review.

Poliakov, A., Cundall, P., Podladchikov, Y. & Lyakhovsky, V., 1993. An explicit inertial method for the simulation of viscoelastic flow: an evaluation of elastic effects on diapiric flow in two- and three-layers model, in *Proceedings of the NATO Advanced Study Institute on Dynamic Modeling and Flow in the Earth and Planets,* pp. 175–195, eds Runcorn, K.E. & Stone, D., Kluwer, Dordrecht.

Poupinet, G., Ellsworth, W.L. & Frechet, J., 1984. Monitoring velocity variations in the crust using earthquake doublets: an application to the Calaveras Fault, California, *J. geophys. Res.,* **89,** 5719—5731.

Rabotnov, Y.N., 1988. *Mechanics of deformable solids,* Moscow, Science, p. 712.

Ranalli, G., 1995. *Rheology of the Earth,* Chapman and Hall Publishers, London.

Regenauer-Lieb, K. & Yuen, D.A., 2003. Modeling shear zones in geological and planetary sciences: solid-and fluid-thermal–mechanical approaches, *Earth-Sci. Rev.,* **63,** 295–349.

Rolandone, F., Burgmann, R. & Nadeau, R.M., 2004. The evolution of the seismic-aseismic transition during the earthquake cycle: constraints from

the time-dependent depth distribution of aftershocks, *Geophys. Res. Lett.,* **31,** L23610, doi:10.1029/2004GL021379.

Rudnicki, J.W. & Rice, J.R., 1975. Conditions for the localization of the deformation in pressure-sensitive, dilatant materials, *J. Mech. Phys. Solids,* **23,** 371–394.

Shcherbakov, R. & Turcotte, D.L., 2004. A modified form of bath's law, *Bull. seism. Soc. Am.,* **94,** 1968–1975.

Shcherbakov, R., Turcotte, D.L. & Rundle, J.B., 2005. Aftershock Statistics, *Pure appl. Geophys.,* **162,** 1051–1076.

Scholz, C.H., 1968. Microfractures, aftershocks, and seismicity, *Bull. seism. Soc. Am.,* **58,** 1117–1130.

Scholz, C.H., 2002. *The mechanics of earthquakes and faulting,* Cambridge University Press, p. 471.

Tsenn, M.C. & Carter, N.L., 1987. Upper limits of power law creep of rocks, *Tectonophysics,* **136,** 1–26.

Turcotte, D.L., Newman, W.I. & Shcherbakov, R., 2003. Micro and macroscopic models of rock fracture, *Geophys. J. Int.,* **152**(3), 718–728.

Utsu, T., 2002. Statistical features of seismicity, in *International Handbook of Earthquake and Engineering Seismology,* pp. 719-732. Part A, eds Lee, W.H.K., Kanamori, H., Jennings, P.C. & Kisslinger, C.

Utsu, Y., Ogata, Y. & Matsu'uara, R.S., 1995. The centenary of the Omori formula for a decay law of aftershock activity, *J. Phys. Earth,* **43,** 1–33.

Vere-Jones, D., Robinson, R. & Yang, W., 2001. Remarks on the accelerated moment release model: problems of model formulation, simulation and estimation, *Geophys. J. Int.,* **144,** 517–531.

Weertman, J., 1978. Creep laws for the mantle of the Earth, *Phil. Trans. R. Soc. Lond A,* **288,** 9–26.

Wiemer, S. & Katsumata, K., 1999. Spatial variability of seismicity parameters in aftershock zones, *J. geophys. Res.,* **104,** 13 135–13 151.

Yamashita, T. & Knopoff, L., 1987. Models of aftershock occurrence, *Geophys. J. R. astr. Soc.,* **91,** 13–26.

Zöller, G., Hainzl, S., Holschneider, M. & Ben-Zion, Y., 2005. Aftershocks resulting from creeping sections in a heterogeneous fault, *Geophys. Res. Lett.,* **32,** L03308, doi:10.1029/2004GL021871.

APPENDIX: MATERIAL STABILITY AND DYNAMIC WEAKENING

Lyakhovsky *et al.* (1997a) define the critical value of damage α_c leading to brittle instability (their eqs 14 and 15) from the conditions for the loss of convexity of the elastic potential (3). When the damage variable reaches α_c, the potential (3) is not convex and a unique solution for the static stress distribution in the elastic material ceases to exist (Ekland & Temam 1976). Similarly to localization of plastic deformation in elasto-plastic models (e.g. Rudnicki & Rice 1975), the loss of convexity in the damage rheology model leads to strain localization along a narrow damage zone (e.g. Hamiel *et al.* 2004). As shown below, elastic waves propagating in a solid with slowly increasing damage are amplified when the damage variable α reaches a value α_d slightly lower than the critical level α_c defined from the convexity consideration. The modified critical value α_d depends on the rate of damage increase and a material parameter governing the weakening timescale. In our simulations, α_c is used to define the initiation of a seismic event, while α_d is used to calculate the (quasi-dynamic) propagation of the event.

In a 1-D case of a damaged solid, the equation for elastic wave propagation is

$$\rho \frac{\partial^2 u}{\partial t^2} + \psi(\alpha) \frac{\partial u}{\partial t} = \frac{\partial}{\partial x}\left(\mu_\alpha \frac{\partial u}{\partial x}\right), \tag{A1}$$

where $u(x, t)$ is displacement, ρ is density, μ_α is the effective elastic modulus of a damaged solid given by $\mu_\alpha = \mu_0(1 - \alpha)$ and $\psi(\alpha)$ is a radiation damping term. We are looking for a travelling wave solution of (A1) in the form

$$u(x, t) = f(t) \cdot \exp(ikx), \tag{A2}$$

where k is wave number. Substituting (A2) into (A1) and assuming gradual spatial variations compared to the disturbance wavelength ($k(\partial \mu_\alpha/\partial x) \ll 1$) leads to equation for $f(t)$ in the form

$$\rho \frac{d^2 f}{dt^2} + \psi(\alpha) \frac{df}{dt} + k^2\mu_\alpha f = 0. \tag{A3}$$

Eq. (A3) has an oscillatory solution with frequency $\omega^2 = k^2\mu_\alpha/\rho$ for slowly changing material properties compared to the wave frequency ($\dot{\alpha}/\omega \ll 1$). The amplitude change during progressive oscillations is proportional to $\exp[-(\dot{\omega}/\omega + \psi/2\rho)t]$ (e.g. Cole 1968). Thus, the travelling waves are damped only if

$$\frac{2\rho}{\psi} < -\frac{\omega}{\dot{\omega}}. \tag{A4}$$

The condition (A4) implies that the characteristic time of the frequency reduction is larger than the characteristic time associated with the damping term. Using the linear relation between the damage variable α and the effective elastic modulus μ_α, the characteristic time of the frequency change is

$$\frac{\omega}{\dot{\omega}} = -\frac{2(1 - \alpha)}{\dot{\alpha}}. \tag{A5}$$

The characteristic time associated with the damping term, or Maxwell timescale, is equal to the ratio between the viscosity and elastic shear modulus. For a constant Newtonian viscosity and degrading elastic modulus, this timescale increases proportionally to $1/(1 - \alpha)$. The singularity at the maximum damage level $\alpha = 1$ becomes stronger in the case of a power-law viscosity $\rho/\psi \sim 1/(1 - \alpha)^n$, where n is the power in a stress vs. strain-rate relation for ductile flow. Adopting for simplicity the Newtonian case and substituting (A5) back to (A4) provides the following condition for stability of the material with quasi-static damage increase,

$$\dot{\alpha} < \frac{(1 - \alpha)^2}{\tau_r}, \tag{A6}$$

where τ_r is a characteristic timescale associated with the damping term in a damage-free material. The condition (A6) could be rewritten in terms of maximum damage α_d satisfying the dynamic stability condition for a given rate of damage increase

$$\alpha_d = 1 - \sqrt{\tau_r\dot{\alpha}}. \tag{A7}$$

Similarly, in the general 3-D case with critical damage α_c defined from the static convexity condition, α_d is

$$\alpha_d = \alpha_c - \sqrt{\tau_r\dot{\alpha}}. \tag{A8}$$

The right term in eq. (A8) may be considered as a dynamic weakening of the material following the occurrence of brittle instability. The damage level α_d is used in our work to perform quasi-dynamic calculations of rupture propagation.